ACS APPLIED MATERIALS & INTERFACES

www.acsami.org

Research Article

Black Au-Decorated TiO_2 Produced via Laser Ablation in Liquid

Stanislav O. Gurbatov, Evgeny Modin, Vladislav Puzikov, Pavel Tonkaev, Dmitriy Storozhenko, Aleksandr Sergeev, Neli Mintcheva, Shigeru Yamaguchi, Natalie N. Tarasenka, Andrey Chuvilin, Sergey Makarov, Sergei A. Kulinich, and Aleksandr A. Kuchmizhak*

Cite This: *ACS Appl. Mater. Interfaces* 2021, 13, 6522–6531

Read Online

ACCESS | Metrics & More | Article Recommendations | Supporting Information

ABSTRACT: The rational combination of plasmonic and all-dielectric concepts within hybrid nanomaterials provides a promising route toward devices with ultimate performance and extended modalities. Spectral matching of plasmonic and Mie-type resonances for such nanostructures can only be achieved for their dissimilar characteristic sizes, thus making the resulting hybrid nanostructure geometry complex for practical realization and large-scale replication. Here, we produced amorphous TiO_2 nanospheres decorated and doped with Au nanoclusters via single-step nanosecond-laser irradiation of commercially available TiO_2 nanopowders dispersed in aqueous $HAuCl_4$. Fabricated hybrids demonstrate remarkable light-absorbing properties (averaged value ≈96%) in the visible and near-IR spectral range mediated by bandgap reduction of the laser-processed amorphous TiO_2 as well as plasmon resonances of the decorating Au nanoclusters. The findings are supported by optical spectroscopy, electron energy loss spectroscopy, transmission electron microscopy, and electromagnetic modeling. Light-absorbing and plasmonic properties of the produced hybrids were implemented to demonstrate catalytically passive SERS biosensor for identification of analytes at trace concentrations and solar steam generator that permitted to increase water evaporation rate by 2.5 times compared with that of pure water under identical 1 sun irradiation conditions.

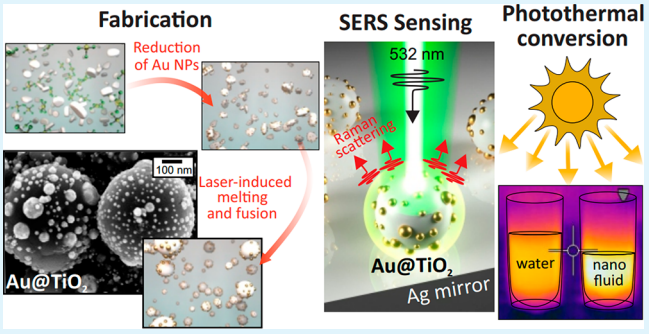

KEYWORDS: *laser ablation in liquid, hybrid nanoparticles, titanium dioxide, gold, plasmonics, SERS, photothermal conversion*

INTRODUCTION

Collective resonant oscillations of conduction electrons (also known as localized surface plasmon resonance (LSPR)) in noble-metal nanoparticles (NPs) provide a common and reliable way to control electromagnetic fields at nanoscale. Such oscillations facilitate resonant absorption of incident energy that can be converted to strongly enhanced electromagnetic field around the NP surface or dissipate via nonradiative damping to induce localized heating. Both electromagnetic and photothermal effects have found numerous practical applications in photovoltaics, solar energy conversion, biomedicine, sensing, and so on.[1−3] Alternatively, NPs made of various materials with high refractive index (high-*n*) and low dissipative losses in the visible and near-IR spectral range (for example, Si, Ge, and TiO_2) emerged recently as alternative platform for nanoscale light management.[4] In particular, such nanomaterials support Mie-type resonances that permit to concentrate electromagnetic energy inside the NP bulk, giving rise to efficient photothermal conversion and highly enhanced nonlinear optical effects.[5−9]

The rational combination of plasmonic and all-dielectric concepts to design hybrid nanostructures is expected to provide a promising route toward advanced nanomaterials with optimized optical response and extended operation range.[10−15] Meanwhile, spectral matching of LSPRs and Mie-type resonances of noble-metal and high-*n* NPs is crucial for optimal performance. Unfortunately, in the visible and near-IR spectral ranges such resonant matching can be achieved for dissimilar characteristic dimensions of both types of NPs (in particular, 100−500 nm for dielectric NPs and <50 nm for plasmonic ones). This makes the NP geometry quite complex for practical realization, even with time- and money-consuming lithography-based techniques.

Laser ablation in liquids (LAL) has emerged as a promising high-performance and green approach for nanomaterial preparation.[16−20] When compared with wet-chemistry methods, LAL represents a simple and environmentally friendly technology that can be performed under normal environmental conditions without external stimuli. Intense pulsed laser

Received: November 18, 2020
Accepted: January 22, 2021
Published: January 27, 2021

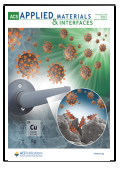

https://dx.doi.org/10.1021/acsami.0c20463
ACS Appl. Mater. Interfaces 2021, 13, 6522−6531

radiation generates extremely high local pressures, temperatures, and quenching rates, thus providing experimental conditions for production of nanostructures with different phase composition (including unique metastable phases),[21,22] complex chemical composition, and morphology.[23−33] However, so far only a few studies reported on LAL-generated hybrid nanomaterials where plasmonic and dielectric counterparts were combined within practically relevant design,[22,34−36] yet without rigorous assessment of their nanophotonic properties and practical applications.

In this paper, amorphous TiO_2 spherical-shaped NPs decorated and doped with Au nanoclusters were produced via single-step ablation of commercially available TiO_2 nanopowders in the presence of $HAuCl_4$ with nanosecond laser pulses. The fabricated hybrids demonstrated broadband light-absorbing properties (averaged value ≈96%) in the visible and near-IR spectral ranges mediated by bandgap reduction of the laser-processed amorphous TiO_2 as well as LSPRs of the decorating Au nanoclusters, which was confirmed by combining optical spectroscopy, advanced EELS/TEM, and electromagnetic modeling. When placed on a back-reflecting mirror, the Au@TiO_2 NPs demonstrated excellent SERS performance resulted from the coupled Mie resonance of TiO_2 spheres and the LSPRs of decorating Au nanoclusters. Isolated Au@TiO_2 NPs were found to provide background-free chemically nonperturbing optical identification of various analytes at initial concentrations down to 10^{-8} M. Au@TiO_2 NPs with their strong broadband optical absorption make them promising for photothermal conversion of the solar energy. As a proof of concept, by using a commercial cellulose membrane functionalized with solar-energy-absorbing Au@TiO_2, we realized a lab-scale water steam generator which permitted to increase evaporation rate by 2.5 times compared with that of pure water.

MATERIALS AND METHODS

Fabrication of Au@TiO_2 Nanoparticles. Two types of commercially available TiO_2 nanopowders (anatase powder from Wako Chemicals, 99.99% pure, and P25 from Degussa, 99.5% pure) with average particle sizes 125 and 21 nm, respectively, were used as supplied. First, NPs were dispersed in deionized water by means of ultrasonication to achieve 0.001% dispersion. Then, the suspension (6.75 mL) was transferred to a quartz cuvette ($3 \times 3 \times 6$ cm^3), and 0.75 mL of aqueous tetrachloroauric acid ($HAuCl_4$, concentration of 10^{-3} M) was added. Finally, the suspension was magnetically stirred and irradiated with focused nanosecond laser pulses (Quantel Ultra 50, with 7 ns, 532 nm, and 20 Hz as pulse width, wavelength, and repetition rate, respectively) for a variable period of time (up to 4 h) at a laser fluence of 20 mJ/cm^2.

Characterization. *Scanning Electron Microscopy (SEM).* SEM images of Au@TiO_2 NPs were obtained at an accelerating voltage of 5 kV and a beam current of 50 pA (Helios NanoLab 450S, Thermo Fisher, USA). A backscattered electron detector was used to achieve atomic-number-sensitive contrast for highlighting Au particles.

To obtain information about the internal structure and composition of the Au@TiO_2 system, the cross sections of NPs produced by focused ion beam (FIB) milling (beam current of 43 pA at an accelerating voltage of 30 kV) were studied via SEM imaging. A platinum layer was locally deposited atop of Au@TiO_2 nanospheres to protect their surface structures during FIB milling (Figure S1).

More detailed characterization of composition and inner structure was performed by using transmission electron microscopy (TEM) combined with electron tomography. For TEM studies, particles were ultrasonicated in acetone for 5 min, and then a 30 μL droplet was placed on a copper grid with lacey carbon. TEM/scanning TEM (STEM) imaging, electron tomography, and STEM-EDX (energy dispersive X-ray spectroscopy, EDAX) chemical mapping experiments were performed at an acceleration voltage of 300 kV (Titan 60-300, Thermo Fisher, USA). The microscope was equipped with a monochromated X-FEG and spectrometer (Quantum GIF, Gatan, USA) which allowed performing electron energy loss spectroscopy (EELS) with energy resolution better than 50 meV. Probing of the surface plasmons around Au NPs was done by means of high-resolution EELS technique combined with STEM image acquisition. In this case, the microscope was tuned at a beam energy of 60 keV in STEM mode. The spectrum images were recorded in the low-loss region, including zero-loss peak. At each pixel of HAADF stem image, an EELS spectrum was stored with the length of 2048 pixels and energy dispersion 0.01 eV/pixel.

Three-dimensional particle morphology was characterized by the electron tomography technique using high angular annular dark-field STEM (HAADF-STEM) imaging mode. The HAADF-STEM mode provides contrast that is strongly dependent on the atomic number (Z^2); thus, Au NPs appear much brighter at HAADF-STEM images as compared to TiO_2. Tomographic tilt series were acquired at the angles between −74° and +74° at 2° tilt step by Tomography 4.0 software (Thermo Fisher) in automatic mode; the dwell time for acquisition was set to 2 s for the images of 2048 × 2048 pixels with the pixel size of 1.3 nm. The fiducial-less tilt-series alignment and tomographic reconstructions with simultaneous iterative reconstruction (SIRT) techniques were done by using in-house Digital Micrograph (Gatan, USA) scripts.[37] Reconstructed volumes had a voxel size of 5.2 nm^3. The intensity-based segmentation with a local threshold criterion and manual supervision was used. Depending on the intensity value of the pixels, they were assumed as belonging to the Au nanoparticles (bright) or TiO_2 sphere (gray). Segmentation of Au and TiO_2 phases, subsequent 3-D rendering, and statistical calculations were done by using Avizo 8.1 software (Thermo Fisher).

Optical and Raman Spectroscopy. The absorption coefficient $A = 1 - R$ was measured in the 200−1700 nm spectral range with an integrating sphere spectrophotometer (Cary Varian 5000) at a spectral resolution of 1 nm. Halogen and deuterium lamps were used as radiation sources for the vis−NIR and UV range, respectively. The bandgap value E_g was determined by the position of the fundamental absorption edge according to the Tauc equation:

$$(\hbar\nu F(R))^{1/n} = B(\hbar\nu - E_g) \quad (1)$$

where $\hbar$ is Planck's constant, ν is the oscillation frequency of electromagnetic waves, B is a constant showing the slope of the linear fit, and $F(R) = (1 - R)^2/2R$ represents the Kubelka−Munk function. The value of the exponent denotes the nature of the interband electronic transitions—for direct allowed transitions it is equal to $n = 1/2$. The basic procedure for Tauc analysis is to acquire optical absorbance data that cover a range of energies below and above the bandgap transition. The E_g value was determined by extrapolating the linear part of the Tauc curve $(\hbar\nu)^{1/n}$ on the $\hbar$-axis.

Raman spectra of pristine TiO_2 NPs, as well as produced and postannealed Au@TiO_2 hybrids, were acquired with a commercial Raman microscope (Alpha WiTec) at 532 nm (2.33 eV). A similar device was used to probe the SERS performance of Au@TiO_2 NPs. The hybrids were functionalized with several types of practically relevant analytes, namely organic dyes (Rhodamine 6G and acridine orange), medical drag (diphendramine hydrochloride), and histological marker molecules (4′,6-diamidino-2-phenylindole dihydrochloride, DAPI). The NPs were added into the 10^{-8} M analyte solutions and stored there for 2 h. Then, suspensions were drop-cast onto a bulk Ag mirror. Alternatively, a similar smooth Ag mirror was stored in analyte solutions for 2 h to prepare a reference substrate. SERS signals were obtained only from isolated NPs on the substrate and averaged over 50 similar measurements for each analyte to account for random distribution of Au nanoclusters. The analytical enhancement factor (AEF) of the SERS signal for each type of analyte was assessed as a ratio of averaged intensity I_{SERS} of the most intense Raman band (1648, 1369, 1002, and 1613 cm^{-1} for Rhodamine 6G, acridine orange, diphendramine, and DAPI, respectively) to the

https://dx.doi.org/10.1021/acsami.0c20463
ACS Appl. Mater. Interfaces 2021, 13, 6522−6531

averaged intensity I_{REF} of the same band measured on a smooth Ag mirror.[38] Both signals were then normalized to laser intensity and exposure time.

FDTD Modeling. Finite-difference time domain calculations (Lumerical Solutions Ltd.) were undertaken to assess plasmonic properties of the Au@TiO_2 hybrids. The structures were excited with linearly polarized broadband source. Exact 3D models of the NPs were reconstructed from the corresponding STEM images produced during the EELS studies. The dispersion functions for Au and TiO_2 were obtained from Palik.[39]

Modeling of Radiation-Induced Heating of Au@TiO_2 Particles. A theoretical description of nanoparticle heating (induced by either solar or laser radiation) was performed numerically with a commercial software package (Comsol Multiphysics). A numerical model was first constructed for a plane wave irradiation of a bare and Au-decorated ellipsoidal TiO_2 NP (the diameter along the long axis is 21 nm) in water. The distribution of electromagnetic field in the simulated volume excited by a single laser pulse (532 nm wavelength and 25 mJ pulse energy) was calculated by solving the wave equation in the frequency domain. Then, the following heat equation in a time domain during the single-pulse irradiation was calculated:

$$\rho C_p(\delta T/\delta t) + \nabla\cdot(-\kappa\nabla T) = \vec{J}\cdot\vec{E} \quad (2)$$

where the right side of this equation describes the heat source with the current density J and electric field amplitude E, whereas the left side corresponds to temperature evolution in time and space with corresponding parameters: C_p is the heat capacity at constant pressure, ρ is the material density, and κ is the thermal conductivity. We suppose the refractive indexes are $n_{Au} = 0.56 + 3.44i$, $n_{water} = 1.335$, and $n_{TiO_2} = 2.54 + 0.0001i$. Thermal conductivities for TiO_2, Au and water are taken as $\kappa_{TiO_2} = 7$ W/(m K), $\kappa_{Au} = 320$ W/(m K), and $\kappa_{water} = 0.6$ W/(m K). A similar procedure was used to calculate heating efficiency of the Au@TiO_2 hybrids of variable diameter in water and on the glass substrate. For these calculations, an excitation source with a central wavelength at 550 nm and an intensity 0.1 W/cm^2 was considered providing reliable approximation of solar irradiation. We defined thermal boundary conditions as a heat flux through the computational domain surface $q = h(T_{ext} - T)$, where h is the heat transfer coefficient, $T_{ext} = 293$ K is the external temperature, and T is the calculated temperature near the boundary of the computational domain. We assumed that temperature gradient is weak because in real experiments there are a lot of particles nearby. From these considerations we estimate value of h equals 0.22 W/(m^2 K).

Water Steam Generation. The nanofluid was prepared by suspending 50 mg of Au@TiO_2 in 10 mL of distilled water. Also, a similar suspension was filtered through a commercial cellulose membrane (pore diameter of 200 nm) and then dried in a vacuum. The produced nanofluid and "black" membrane loaded with Au@TiO_2 NPs were placed on the surface of distilled water and irradiated by a commercial solar simulator at 0.1 W/cm^2. A microbalance was used to detect weight loss of water after evaporation. The evaporation rate observed in both cases was compared with that of distilled water. The heating process was visualized with a calibrated IR camera. All experiments were performed at 25 °C and a relative humidity of 40%.

RESULTS AND DISCUSSION

Black Au-Decorated TiO_2: Fabrication and Structural Properties. Figure 1a schematically illustrates key processes that contributed to the formation of Au@TiO_2 NPs by using the LAL technique. In our experiments, aqueous suspension of as-supplied TiO_2 NPs (mainly anatase, average sizes of either 21 or 125 nm) mixed with aqueous solution of $HAuCl_4$ was irradiated by nanosecond laser pulses for a few hours, resulting in formation of spherical TiO_2 decorated with multiple nanosized Au clusters (Figure 1b). Typically, the average size of resulting Au@ TiO_2 hybrids was always larger than the size

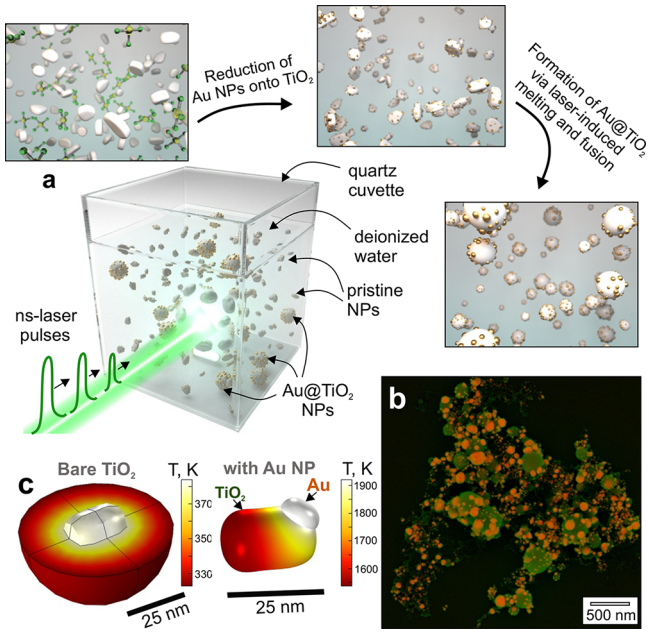

Figure 1. Fabrication of Au@TiO_2 NPs via laser ablation in liquid. (a) Schematic representation of fabrication process based on direct irradiation of a stirred water suspension of TiO_2 NPs with nanosecond laser pulses. Insets explain relevant processes involved in the formation of Au@TiO_2 NPs. (b) Representative false-color SEM image of NPs produced upon irradiation of the suspension containing 21 nm sized TiO_2 NPs for 2 h at a pulse energy of 20 mJ/cm^2 and a pulse repetition rate of 20 Hz. (c) Calculated temperature profile in the vicinity of a bare and Au-decorated TiO_2 NP upon irradiation with a single nanosecond laser pulse at 20 mJ/cm^2. Bare TiO_2 NP is shown inside the water medium.

of precursor titania NPs (for both types of nanopowders used). Accordingly, the observed increase in size and spherical shape of produced NPs indicate melting and fusion as key processes involved in their formation.

However, the as-supplied crystalline TiO_2 NPs of both types are expected to absorb visible light weakly, which results in their single-pulse laser heating that is insufficient to reach the melting point of bulk TiO_2 (≈1900 K,[40]). In particular, a 21 nm sized TiO_2 NP suspended in water can be homogeneously heated to only 385 K upon irradiation with a single 7 ns laser pulse at fluence of 20 mJ/cm^2, as confirmed by corresponding numerical modeling (see Figure 1c and the Methods section for simulation details). In a sharp contrast, Au NPs that are smaller than 50 nm can efficiently absorb the corresponding laser irradiation that in general is close to the wavelength of their localized plasmon resonance. The absorbed radiation is then converted to Joule heating by resonantly excited conduction electrons, while the generated heat can be further transferred to the environment. Similar modeling of single-pulse laser heating of an isolated 21 nm large TiO_2 NP decorated with an Au cluster with its diameter of 5 nm shows that such a hybrid nanostructure can easily reach temperatures exceeding 1900 K at the same fluence of laser irradiation (Figure 1c). Note that the heat dissipation from the NPs to environment leads to a certain increase of the average temperature of the suspension to 33 °C upon its irradiation for 4 h, which was detected by an embedded temperature sensor (Figure S2).

To further support this idea, LAL experiments were performed with similar suspensions of pristine TiO_2 NPs at

https://dx.doi.org/10.1021/acsami.0c20463
ACS Appl. Mater. Interfaces 2021, 13, 6522−6531

the same laser fluence and irradiation time but without addition of $HAuCl_4$. Careful SEM analysis of obtained products indicated no modification/melting of pristine NPs revealing the key role of Au nanoclusters decorating TiO_2 NPs. The formation of such Au NPs can occur even without laser irradiation and is expected to be preferentially facilitated on TiO_2 NPs via surface chemistry driven by active sites and laser-induced enhanced temperature near NP's surface.

As mentioned above, after irradiation for 2 h all as-supplied TiO_2 NPs with irregular shapes were transformed to spherically shaped Au@TiO_2 hybrids. For both types of used pristine NPs with their average sizes of 21 (or 125 nm), the obtained hybrids had the averaged diameters of 120 (or 220 nm), respectively, indicating that fusion of several NPs was involved (see Figure 2, middle). A shorter irradiation time

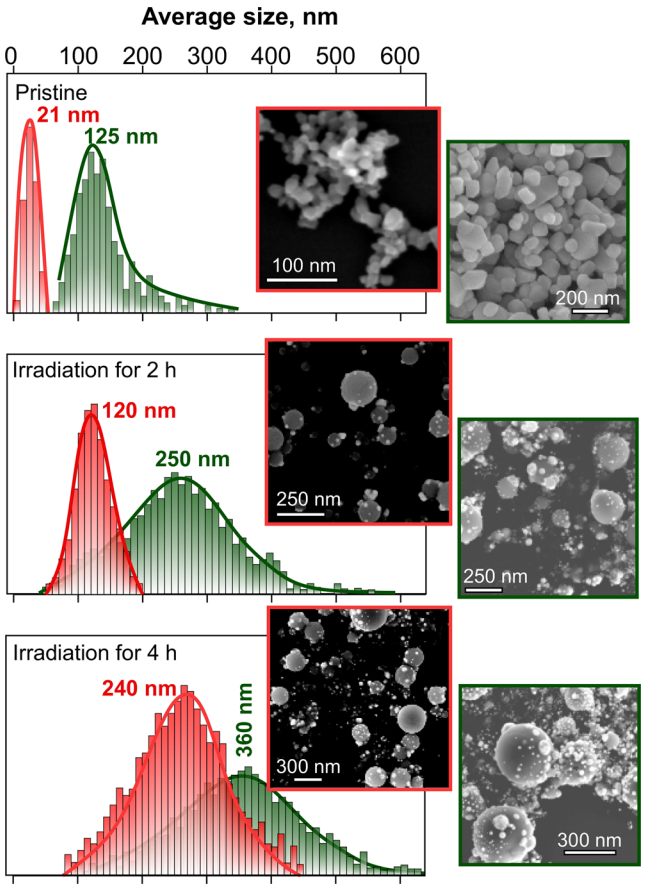

Figure 2. Tailoring the size of Au@TiO_2hybrids. Size distribution measured for pristine TiO_2 NPs of both types (top) and Au@TiO_2 products obtained from these NPs after irradiation for 2 and 4 h (middle and bottom). Each size distribution is illustrated by representative SEM images.

resulted in the particular presence of pristine TiO_2 NPs in the obtained product. Further irradiation of the TiO_2 suspension for 4 h yielded in even larger size of obtained Au@TiO_2 hybrids (Figure 2, bottom). The number of adsorbed Au nanoclusters and their size were also found to increase with laser irradiation time as well as with the concentration of $HAuCl_4$ in the irradiated dispersion. From practical application point of view, it is important to control both the average size of the spherically shaped TiO_2 NPs and their decoration degree. We found that by varying the starting size of pristine TiO_2 NPs, irradiation time, and $HAuCl_4$ concentration, both parameters could be independently controlled. The related information is summarized in Figure 2 and Figure S3.

High-resolution TEM was used to identify crystallinity of the obtained Au@TiO_2 product. TEM images of representative NPs are shown in Figure 3a–d, revealing completely

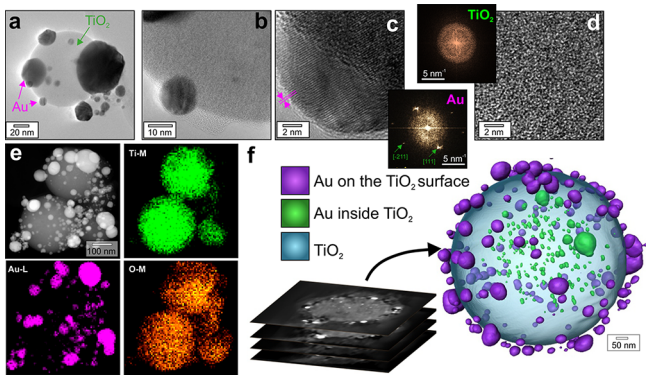

Figure 3. Structure and composition of laser-fabricated Au@TiO_2NPs. (a, b) Representative TEM images of Au@TiO_2 NPs. (c, d) HR-TEM images showing crystalline structure of an isolated Au nanocluster and TiO_2 NP. Insets show the corresponding FFT images. (e) EDX chemical composition mapping of Au@TiO_2 NPs. (f) 3D model of an Au@TiO_2 NP reconstructed by using tomographic series of HAADF-STEM images. For clarity, Au NPs situated on the surface and inside the TiO_2 nanosphere are highlighted by purple and green colors, respectively.

disordered structure in the TiO_2 nanosphere and crystalline structure of the decorating Au nanoclusters. FFT analysis of the selected HR-TEM images confirmed amorphous nature of TiO_2 nanospheres (insets in Figure 3c,d). Additionally, Raman spectroscopy was utilized to provide more information regarding the crystallinity of TiO_2 statistically averaged over multiple NPs before and after LAL processing. These studies permitted clearly to identify all main anatase Raman bands for both types of as-supplied TiO_2 NPs and low-intensity bands at 440 and 610 cm^{-1} that can be attributed to a small amount of nanocrystalline rutile inclusions in the Au@TiO_2 product (Figure S4). EDX mapping was used to confirm chemical composition of the Au@TiO_2 NPs (Figure 3e).

The formation mechanism suggests that Au NPs that stimulated TiO_2 melting can appear not only on the surface of Au@TiO_2 product but also in its bulk. Indeed, the average size of Au@TiO_2 product is much larger compared with the size of pristine TiO_2 used for its fabrication. This indicates that fusion of several pristine NPs is required to form a hybrid one. Moreover, fusing TiO_2 NPs can contain Au nanoclusters on their surface, which would allow gold to penetrate inside and dope the Au@TiO_2 hybrids. To clarify this, several FIB cross-sectional cuts of Au@TiO_2 were first visualized by using SEM revealing high-contrast nanoscale inclusions that appeared much brighter compared with TiO_2 surrounding and could be attributed to Au (see Figure S1). More detailed studies of the inner structures of Au@TiO_2 NPs were performed via tomographic reconstruction of HAADF-STEM image series (see the Methods section for details).

The reconstructed 3D model of an isolated Au@TiO_2 NP is shown in Figure 3f, where Au nanoclusters located on the surface and inside the TiO_2 NP are highlighted by different colors for clarity. Systematic studies of the produced Au@TiO_2

https://dx.doi.org/10.1021/acsami.0c20463
ACS Appl. Mater. Interfaces 2021, 13, 6522–6531

hybrids indicated that the inner Au nanoclusters occupy ≈0.5−1% of the volume of TiO_2 nanosphere. Noteworthy, such Au nanoclusters both embedded into TiO_2 NPs and simultaneously decorating their surface are reported for the first time.

Optical and Plasmonic Properties of Au@TiO_2 Hybrids. Plasmonic response of Au nanoclusters capping amorphous spherical-shaped TiO_2 was first probed by high-resolution EELS. A representative EELS spectrum measured from an isolated Au nanocluster sitting on the surface of a 225 nm sized spherical TiO_2 NP demonstrates a pronounced split peak around 2.3 eV (Figure 4a), with the red component at 2.1 eV and the blue one at 2.4 eV. Mapping of the intensity of this signal (1.9−2.5 eV) confirmed that it originates from the Au nanocluster surface (Figure 4b). EELS signals at 5.7 and 10 eV are known low-loss peaks of TiO_2.

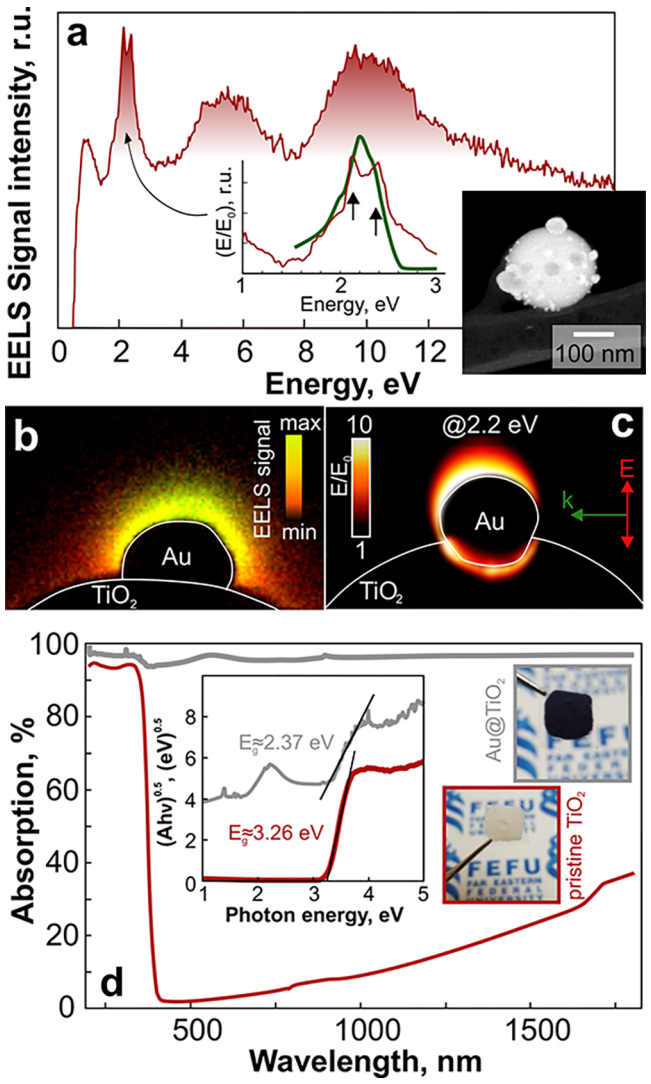

Figure 4. Optical properties of Au-decorated black TiO_2NPs. (a) High-resolution EELS spectrum of isolated Au nanocluster capping the TiO_2 NP surface. The reference TEM image is shown as an inset. The bottom inset provides close-up look at the EELS spectrum near the plasmon resonance feature superimposed with a calculated averaged near-field plasmonic spectrum of the Au nanocluster (green dashed curve). (b) EELS map showing signal intensity in the spectral range from 1.9 to 2.4 eV. (c) Normalized EM-field amplitude E/E_0 calculated at 2.1 eV pump. (d) Absorption spectra of pristine TiO_2 and Au@TiO_2-based opaque coatings covering the glass slide. The insets show a Kubelka−Munk representation of the absorption spectra with an indication of bandgap E_g for Au@TiO_2 and pristine TiO_2 as well as the optical images of both samples.

The size of the considered Au nanocluster is comparable with a doubled skin depth of gold (≈ 30 nm), thus suggesting that the dipolar approximation is applicable for formal analysis of its plasmon modes. Considering the dielectric permittivity of Au, the localized dipolar plasmon resonance of such a NP in a vacuum should appear around 2.35 eV, red-shifting to 2.1 eV when it attaches a high-refractive-index TiO_2 surface. Also, the shape of the obtained Au nanoclusters (grown above or even penetrating into their TiO_2 support) is typically irregular, suggesting a certain broadening of the localized plasmon resonances. The resonance seen at 2.365 eV can be attributed to the quadrupolar localized plasmonic modes appearing because of the substrate-induced red-shift of the dipolar one. These inferences are consistent with the supporting FDTD calculations showing the near-field plasmonic spectrum of the slightly elliptical Au nanocluster capping TiO_2 NP as well as the normalized amplitude of the electromagnetic near fields under resonant excitation (at 2.1 eV; Figure 4a,c). Statistical EELS studies averaged over various Au clusters found on TiO_2 spheres indicate that the Au@TiO_2 hybrids support localized plasmons in a rather broad spectral range spanning from 500 to 650 nm. Moreover, closely spaced Au clusters can act as plasmonic oligomers with their resonance shifted to the near-IR part of the spectrum (see Figure S5).

In addition, we assessed optical properties of Au@TiO_2 hybrids in the visible and near-IR part of their spectra (Figure 4d). For this purpose, the Au@TiO_2 suspension produced by laser irradiation of the pristine TiO_2 (P25 from Degussa) for 4 h was dried on a cover glass slide to form a uniform opaque coating. In a sharp contrast to the similar coating made of both types of pristine TiO_2 NPs, the color of the Au@TiO_2 nanomaterial appeared black, indicating high absorption in the visible spectral range.

Corresponding measurements of absorption coefficient ($A = 1 - R$; R = diffuse reflectance) of both coatings revealed an order of magnitude larger vis-to-IR absorption by the "black" Au-decorated amorphous TiO_2 with respect to its "white" pristine precursors. On the basis of the obtained diffuse reflectance, we found a considerable decrease of the bandgap E_g value from 3.26 eV (pristine TiO_2) to 2.37 eV (Au@TiO_2 hybrids) for direct transitions according to the Kubelka−Munk method (see the inset in Figure 4d). Noteworthy, the maximal absorption (≈97.7%) mediated by the localized plasmon resonances of the Au nanoclusters capping TiO_2 was observed near 2.2 eV, which is consistent with the numerical modeling and EELS studies. Noteworthy, both reshaping of the TiO_2 NPs accompanied by their transformation from crystalline to amorphous state and their decoration/doping with Au nanoclusters contribute to strong and broadband light absorption. To support this statement, we studied optical properties of similar dried NP films that contained pristine TiO_2 nanomaterial mixed with Au NPs in a similar proportion as it was obtained in Au@TiO_2 hybrids (Figure S6).

Use of Au@TiO_2 Hybrids for Label-Free Biosensing and Photothermal Conversion. The observed remarkable optical and plasmonic properties of the prepared Au@TiO_2 hybrids suggest several areas for their potential application. First of all, the plasmon-mediated EM field localized near Au nanoclusters make such Au@TiO_2 hybrids attractive for label-free biosensing based on the surface-enhanced Raman

https://dx.doi.org/10.1021/acsami.0c20463
ACS Appl. Mater. Interfaces 2021, 13, 6522−6531

scattering (SERS) effect. As the electromagnetic contribution to the SERS signal is predominant roughly scaling as fourth power of the local electromagnetic field amplitude normalized over the pump field amplitude E^4/E_0^4, maximization of this value gives a general route for boosting SERS performance. Au nanoclusters produce enhanced plasmon-mediated EM fields under resonant visible-light excitation. However, the nanoscale size of such particles results in their low absorption cross section. As a result, they efficiently interact only with a small fraction of incident pump laser beam with a diffraction limited lateral size typical for SERS experiments. In the produced Au@TiO_2 hybrids, the excitation of decorating Au particles can be improved via additional coupling of the incident field to the Mie resonances supported by TiO_2 spheres with diameters comparable with the diffraction-limited ($\approx \lambda/2$) laser spot.[15,41] To illustrate this, we performed FDTD calculations showing a 2-fold increase of the local E/E_0 amplitude near an isolated Au particle upon its attachment to a 240 nm sized TiO_2 sphere supporting magnetic-type dipolar resonance matching the dipolar LSPR. Such improvement permits to expect contribution to SERS electromagnetic enhancement that is at least an order of magnitude larger compared to those from a similar isolated Au particle in a free space.

Additionally, the geometry of the prepared Au@TiO_2 hybrids permits to apply them with back-reflector mirror.[42] In our case, this concept can be simply realized upon SERS studies by placing Au@TiO_2 NPs on a smooth refectory mirror. In this respect, the TiO_2 sphere acts as a support for Au nanoclusters providing required gap between plasmonic NPs and reflecting mirror. Corresponding FDTD calculations of the local EM field enhancement gave more than a 3-fold enhancement of E/E_0 (compared with the case of Au particle in a free-space) near the isolated Au nanocluster, yielding in further increase of the SERS performance (Figure 5a–c). The amorphous structure of TiO_2 spheres contributed to the background-free SERS studies.

To assess the applicability of Au@TiO_2 hybrids for reliable label-free optical identification at trace concentrations, we probed the SERS signal from isolated NPs with an average diameter 240 ± 20 at the 532 nm (2.33 eV) pumping wavelength. The Au@TiO_2 NPs were functionalized with several types of practically relevant analytes, namely organic dyes (Rhodamine 6G and acridine orange), medical drags (diphendramine hydrochloride), and histological marker molecules (DAPI). Considering the rather random size distribution and arrangement of decorating Au nanoclusters, for each type of the analyte we statistically averaged the SERS signal over at least 50 NPs, performing measurements only from isolated structures. By laser pumping isolated Au@TiO_2 NPs stored in the analyte solution for 2 h and then drop-cast onto a silver mirror, we found distinct SERS signals from all tested analytes (Figure 5d). The spectral positions of the identified Raman bands were found to be in good agreement with previously reported studies substantiating isolated Au@TiO_2 hybrids as simple all-in-one SERS platforms with optimized EM response for reliable fingerprinting at initial concentrations down to 10^{-8} M (Figure 5e–h). By comparing the SERS signal from analytes on a smooth Ag mirror (see Materials and Methods), we estimated AEF of the single-nanoparticle SERS probe to be 1.5×10^6, 0.95×10^6, 0.32×10^6, and 0.89×10^6 for Rhodamine 6G, acridine orange, diphenhydramine, and DAPI, respectively. The electromagnetic contribution to the SERS signal enhancement is expected

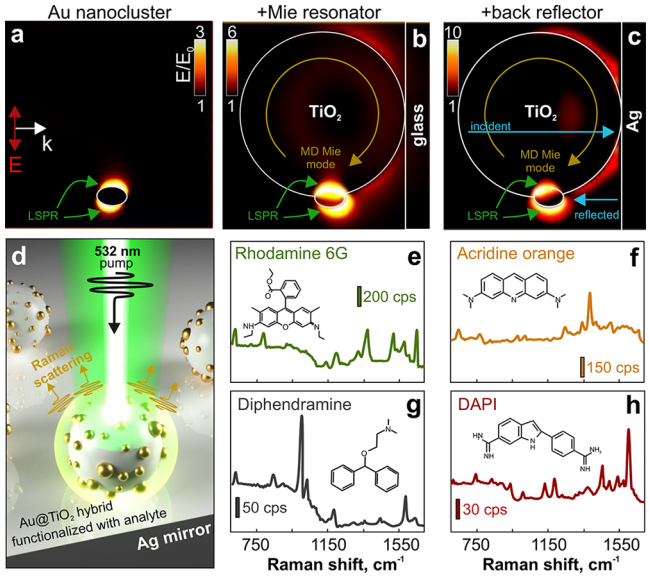

Figure 5. SERS performance of the Au@TiO_2 hybrids on a back-reflecting mirror. Average enhancement of the electromagnetic field amplitude E/E_0 calculated for isolated Au NP in a free space (a) as well as Au NP attached to a 240 nm sized TiO_2 sphere on a glass (b) and Ag substrate (c). (d) Schematic illustration of SERS probe based on an isolated Au@TiO_2 hybrid placed on the Ag mirror. Series of averaged SERS spectra of Rhodamine 6G (e), acridine orange (f), Diphendramine (g), and DAPI (h).

to be dominant in these experiments, as the obtained AEF is generally on the order of $(E/E_0)^4$ calculated for isolated Au nanoclusters placed on a surface of a Mie resonant TiO_2 nanosphere. Our supporting calculations also showed that electromagnetic contribution from closely spaced Au nanoclusters supporting gap plasmons is expected to be weak (Figure S7). The difference in the AEF for various analytes can be explained by their different chemical affinity to both the Au@TiO_2 hybrids and reference substrate.[43] In addition, several papers reported that charge transfer between Au and TiO_2 can also contribute to the overall SERS yield from attached molecules.[44−47] Noteworthy, NPs for SERS studies provide additional flexibility for device designs. For example, quantitative SERS measurements using NPs can be performed in liquids to detect and trace catalytic processes.[48] Moreover, the analyte solution loaded with functional NPs can be dried on a substrate with specially designed wetting properties. After solvent evaporation on such a surface, the deposition area for both the molecules and functional NPs will be substantially reduced, increasing the local concentration of the analyte already mixed with SERS-active probes.[49−51] Realization of such NP-based sensor active device will become a subject of our forthcoming studies.

Moreover, several studies highlighted the excellent catalytic performance of laser-modified titania again visible-light driven degradation of dye molecules.[52] In this work we used two common oppositely charged methylene blue and methylene orange organic dye molecules to benchmark photocatalytic activity of the produced Au@TiO_2 hybrids (see Figure S8). Remarkably, in comparison to the as-supplied pristine TiO_2 (P25 from Degussa), the Au@TiO_2 hybrids with amorphous core demonstrate more than an order of magnitude weaker activity in photocatalytic degradation of both dye molecules. Noteworthy, weak photocatalytic activity of the nanostructures

https://dx.doi.org/10.1021/acsami.0c20463
ACS Appl. Mater. Interfaces 2021, 13, 6522−6531

is beneficial in designing SERS substrates for studies where noninvasive and nonperturbing identification of analytes is mandatory.[48] It should be noted that postannealing of the Au@TiO_2 product can be used to convert its amorphous core to rutile crystalline phase. Raman spectroscopy indicated the appearance of characteristic rutile bands (at 445 and 610 cm^{-1}) in Au@TiO_2 hybrids after their annealing at 500 °C for 2 h (see Figure S4). However, more detailed studies of postannealing of Au@TiO_2 NPs and its effect on crystalline structure and photocatalytic activity of the product are beyond the scope of this paper.

Finally, the excellent broadband optical absorption of the prepared Au@TiO_2 NPs makes them promising for photothermal conversion of the solar energy. In particular, the maximal visible light absorption (≈98%) of Au@TiO_2 nanomaterial mediated by the localized plasmon resonances in Au nanoclusters was observed at 2.2 eV, which perfectly matches the maximum of the solar energy spectrum. Our numerical calculations showed that Au@TiO_2 NPs with diameters ranging from 300 to 500 nm in the form of water suspensions or continuous coatings on a substrate can be efficiently heated under optical excitation that is close to 1 sun irradiation conditions (Figure 6a). The importance of the Au nanoclusters doping and incorporating the TiO_2 NPs in the process of photothermal conversion is highlighted by similar thermal calculations made for pure TiO_2 spheres of variable diameters. Thus, local heating provided by Au@TiO_2 NPs allows for fast liquid−vapor phase transition that can be applied for steam generation or water desalination.[53−56]

We performed comparative experiments run with a custom-built solar simulator heating the black Au@TiO_2 product and pristine white TiO_2 material arranged to form "FEFU" letters under 1 sun irradiation (≈ 0.1 W/cm^2). These experiments showed that the black Au@TiO_2 coating reaches a maximal temperature of about 60 °C within 5 min, in a sharp contrast with white TiO_2 reaching only 35 °C as indicated by temperature measurements with a calibrated IR camera (see Figure 6b,c). In addition, by using the Au@TiO_2 product, we realized a lab-scale water steam generator based on both localized and volumetric heating approaches (Figure 6d). To do this, the weight loss of water during evaporation under 1 sun irradiation (at 0.1 W/cm^2) was monitored and evaluated for the Au@TiO_2-based nanofluid and cellulose-membrane functionalized Au@TiO_2 NPs (Figure 6d). For both approaches, we found that the evaporation rate increases up to 2.5 times (≈ 1.25 kg m^{-2} h^{-1}) compared with that for pristine distilled water (≈ 0.49 kg m^{-2} h^{-1}), implying the potential applicability of light-absorbing Au@TiO_2 for solar steam generation and water desalination. The interested reader is redirected to the Supporting Information (Figure S9) where we surveyed and compared evaporation performance of several promising light-absorbing nanomaterials utilized for both volumetric and localized heating. Additional information about the topic can be found in several recently published reviews.[54,57−59]

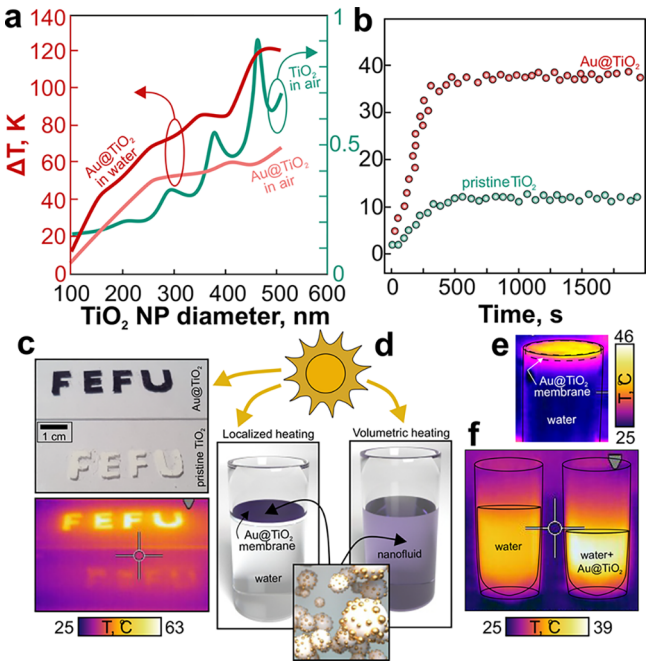

Figure 6. Photothermal conversion with Au@TiO_2hybrids. (a) Calculated temperature increase ΔT in the vicinity of pure TiO_2 (blue curve) and Au@TiO_2 spherical-shaped NPs (red curves) of variable diameter D in water and on a glass substrate under conditions close to 1 sun irradiation. (b) Measured temperature increase of the coatings made of black Au@TiO_2 product and pristine white TiO_2 material. (c) Optical and IR thermal images of corresponding coatings arranged to form "FEFU" letters. (d) Schematic illustration of volumetric and localized heating with Au@TiO_2 hybrids. (e, f) Comparative thermal images of bare distilled water, Au@TiO_2-based nanofluid, and distilled water capped with an Au@TiO_2 membrane.

CONCLUSIONS

To summarize, we have developed a novel approach for the production of multifunctional amorphous TiO_2 nanospheres simultaneously decorated and doped with Au nanoclusters via single-step nanosecond laser ablation of commercially available TiO_2 nanopowders dispersed in the presence of aqueous $HAuCl_4$. The fabricated hybrids demonstrate remarkable light-absorbing properties (averaged value ≈96%) in the visible and near-IR spectral range mediated by bandgap reduction of the laser-processed amorphous TiO_2, as well as LSPRs of the decorating Au nanoclusters, which was confirmed by combining optical spectroscopy, advanced EELS/TEM, and electromagnetic modeling. Excellent light-absorbing and plasmonic properties of the produced hybrids were implemented to demonstrate catalytically passive SERS biosensing for identification of analytes at trace concentration as well as a solar steam generator that permits to increase the water evaporation rate by 2.5 times compared with that of pure water under identical 1 sun irradiation conditions. We also envision that the produced Au@TiO_2 product will be useful as transport layers in third-generation solar cells, for which our NPs possess excellent optical properties, low cost, and the ability to be deposited by scalable wet-chemistry approaches. Similarly, the developed nanomaterials, being mixed with a binder, can be further used for production of highly adhesive ultrablack coatings for optical devices where even weak reflections are highly undesirable.

ASSOCIATED CONTENT

Supporting Information

The Supporting Information is available free of charge at https://pubs.acs.org/doi/10.1021/acsami.0c20463.

https://dx.doi.org/10.1021/acsami.0c20463
ACS Appl. Mater. Interfaces 2021, 13, 6522−6531

Figure S1: SEM image of FIB cross-sectional cuts of neighboring Au@TiO_2 NPs revealing their inner structure; Figure S2: measurements of heat transfer from the nanoparticles to liquid environment during LAL; Figure S3: additional SEM images showing tunability of decoration degree of Au@TiO_2 NPs; Figure S4: crystalline structure of the Au@TiO_2 nanoparticles revealed by Raman spectroscopy; Figure S5: near-IR plasmon resonances in Au nanoparticle agglomerates revealed by EELS; Figure S6: absorption of a mixture of pristine TiO_2 and Au nanoparticles; Figure S7: SERS enhancement provided by Au nanocluster dimer on a TiO_2 nanosphere surface; Figure S8: photocatalytic activity of Au@TiO_2 hybrids; Figure S9: overview of evaporation performance of various nanomaterials (PDF)

AUTHOR INFORMATION

Corresponding Author

Aleksandr A. Kuchmizhak − *Institute of Automation and Control Processes, Far Eastern Branch, Russian Academy of Science, Vladivostok 690041, Russia;* orcid.org/0000-0002-5376-5555; Email: alex.iacp.dvo@mail.ru

Authors

Stanislav O. Gurbatov − *Far Eastern Federal University, Vladivostok 690922, Russia; Institute of Automation and Control Processes, Far Eastern Branch, Russian Academy of Science, Vladivostok 690041, Russia*

Evgeny Modin − *CIC nanoGUNE BRTA, E-20018 Donostia - San Sebastian, Spain*

Vladislav Puzikov − *Far Eastern Federal University, Vladivostok 690922, Russia*

Pavel Tonkaev − *ITMO University, St. Petersburg 197101, Russia*

Dmitriy Storozhenko − *Institute of Automation and Control Processes, Far Eastern Branch, Russian Academy of Science, Vladivostok 690041, Russia*

Aleksandr Sergeev − *Institute of Automation and Control Processes, Far Eastern Branch, Russian Academy of Science, Vladivostok 690041, Russia;* orcid.org/0000-0002-8294-865X

Neli Mintcheva − *Department of Chemistry, University of Mining and Geology, 1700 Sofia, Bulgaria; Research Institute of Science and Technology, Tokai University, Hiratsuka, Kanagawa 259-1292, Japan*

Shigeru Yamaguchi − *Department of Physics, Tokai University, Hiratsuka, Kanagawa 259-1292, Japan*

Natalie N. Tarasenka − *B. I. Stepanov Institute of Physics, 220072 Minsk, Belarus*

Andrey Chuvilin − *CIC nanoGUNE BRTA, E-20018 Donostia - San Sebastian, Spain; IKERBASQUE, Basque Foundation for Science, E-48013 Bilbao, Spain*

Sergey Makarov − *ITMO University, St. Petersburg 197101, Russia;* orcid.org/0000-0002-9257-6183

Sergei A. Kulinich − *Far Eastern Federal University, Vladivostok 690922, Russia; Research Institute of Science and Technology, Tokai University, Hiratsuka, Kanagawa 259-1292, Japan;* orcid.org/0000-0002-1365-9221

Complete contact information is available at: https://pubs.acs.org/10.1021/acsami.0c20463

Author Contributions

S.O.G. and V.P. produced Au@TiO_2 nanomaterial via LAL. P.T. and S.M. modeled heating of the nanoparticle under solar irradiation. D.S. performed electromagnetic modeling and simulated heating of single nanoparticle under laser irradiation. A.S. performed optical spectroscopic characterization. N.M. and S.Y. performed photothermal experiments. E.M. and A.C. performed SEM, TEM, and EDX studies. N.N.T. and S.A.K. performed SERS experiments. A.A.K. supervised the project and wrote the draft together with S.A.K. and S.M. All authors contributed to the revision of the manuscript and approved its final version.

Notes

The authors declare no competing financial interest.

ACKNOWLEDGMENTS

Laser-related experiments, experimental characterization, and sensing experiments were supported by the Russian Science Foundation (grant 19-79-00214). S.G. and S.M. express their gratitude to the Ministry of Science and Higher Education of the Russian Federation (grants M-4321.2021.1.2 and MK-3514.2019.2) regarding performed calculations of temperature profile and light-to-heat conversion efficiency.

REFERENCES

(1) Giannini, V.; Fern'andez-Dom'ınguez, A. I.; Heck, S. C.; Maier, S. A. Plasmonic Nanoan- tennas: Fundamentals and Their Use in Controlling the Radiative Properties of Nanoemitters. *Chem. Rev.* **2011**, *111*, 3888−3912.

(2) Atwater, H. A.; Polman, A. Plasmonics for Improved Photovoltaic Devices. *Nat. Mater.* **2010**, *9*, 205−213.

(3) Baffou, G.; Cichos, F.; Quidant, R. Applications and Challenges of Thermoplasmonics. *Nat. Mater.* **2020**, *19*, 946−958.

(4) Kuznetsov, A. I.; Miroshnichenko, A. E.; Brongersma, M. L.; Kivshar, Y. S.; Luk'yanchuk, B. Optically Resonant Dielectric Nanostructures. *Science* **2016**, *354*, No. aag2472.

(5) Alessandri, I.; Lombardi, J. R. Enhanced Raman Scattering with Dielectrics. *Chem. Rev.* **2016**, *116*, 14921−14981.

(6) Makarov, S. V.; Petrov, M. I.; Zywietz, U.; Milichko, V.; Zuev, D.; Lopanitsyna, N.; Kuksin, A.; Mukhin, I.; Zograf, G.; Ubyivovk, E.; Smirnova, D. A.; Starikov, S.; Chichkov, B. N.; Kivshar, Y. S. Efficient Second-Harmonic Generation in Nanocrys- talline Silicon Nanoparticles. *Nano Lett.* **2017**, *17*, 3047−3053.

(7) Zograf, G. P.; Petrov, M. I.; Zuev, D. A.; Dmitriev, P. A.; Milichko, V. A.; Makarov, S. V.; Belov, P. A. Resonant Nonplasmonic Nanoparticles for Efficient Temperature-Feedback Optical Heating. *Nano Lett.* **2017**, *17*, 2945−2952.

(8) Mitsai, E.; Naffouti, M.; David, T.; Abbarchi, M.; Hassayoun, L.; Storozhenko, D.; Mironenko, A.; Bratskaya, S.; Juodkazis, S.; Makarov, S.; Kuchmizhak, A. Si_{1-x} Ge_x Nanoantennas with a Tailored Raman Response and Light-to-Heat Conversion for Advanced Sensing Applications. *Nanoscale* **2019**, *11*, 11634−11641.

(9) Koshelev, K.; Kruk, S.; Melik-Gaykazyan, E.; Choi, J.-H.; Bogdanov, A.; Park, H.-G.; Kivshar, Y. Subwavelength Dielectric Resonators for Nonlinear Nanophotonics. *Science* **2020**, *367*, 288−292.

(10) Jiang, R.; Li, B.; Fang, C.; Wang, J. Metal/Semiconductor Hybrid Nanostructures for Plasmon-Enhanced Applications. *Adv. Mater.* **2014**, *26*, 5274−5309.

(11) Zuev, D. A.; Makarov, S. V.; Mukhin, I. S.; Milichko, V. A.; Starikov, S. V.; Moro- zov, I. A.; Shishkin, I. I.; Krasnok, A. E.; Belov, P. A. Fabrication of Hybrid Nanostructures via Nanoscale Laser-Induced Reshaping for Advanced Light Manipulation. *Adv. Mater.* **2016**, *28*, 3087−3093.

(12) Sygletou, M.; Tzourmpakis, P.; Petridis, C.; Konios, D.; Fotakis, C.; Kymakis, E.; Stratakis, E. Laser Induced Nucleation of Plasmonic

Nanoparticles on Two-Dimensional Nanosheets for Organic Photovoltaics. *J. Mater. Chem. A* **2016**, *4*, 1020−1027.
(13) Timpu, F.; Hendricks, N. R.; Petrov, M.; Ni, S.; Renaut, C.; Wolf, H.; Isa, L.; Kivshar, Y.; Grange, R. Enhanced Second-Harmonic Generation from Sequential Capillarity-Assisted Particle Assembly of Hybrid Nanodimers. *Nano Lett.* **2017**, *17*, 5381−5388.
(14) Makarov, S. V.; Zalogina, A. S.; Tajik, M.; Zuev, D. A.; Rybin, M. V.; Kuchmizhak, A. A.; Juodkazis, S.; Kivshar, Y. Light-Induced Tuning and Reconfiguration of Nanophotonic Structures. *Laser & Photonics Reviews* **2017**, *11*, 1700108.
(15) Milichko, V. A.; Zuev, D. A.; Baranov, D. G.; Zograf, G. P.; Volodina, K.; Krasilin, A. A.; Mukhin, I. S.; Dmitriev, P. A.; Vinogradov, V. V.; Makarov, S. V.; Belov, P. A. Metal-Dielectric Nanocavity for Real-Time Tracing Molecular Events with Temperature Feedback. *Laser & Photonics Reviews* **2018**, *12*, 1700227.
(16) Amendola, V.; Meneghetti, M. Laser Ablation Synthesis in Solution and Size Manipulation of Noble Metal Nanoparticles. *Phys. Chem. Chem. Phys.* **2009**, *11*, 3805−3821.
(17) Zeng, H.; Du, X.-W.; Singh, S. C.; Kulinich, S. A.; Yang, S.; He, J.; Cai, W. Nanomaterials via Laser Ablation/Irradiation in Liquid: a Review. *Adv. Funct. Mater.* **2012**, *22*, 1333−1353.
(18) Zhang, D.; Gokce, B.; Barcikowski, S. Laser Synthesis and Processing of Colloids: Fundamentals and Applications. *Chem. Rev.* **2017**, *117*, 3990−4103.
(19) Petridis, C.; Savva, K.; Kymakis, E.; Stratakis, E. Laser Generated Nanoparticles Based Photovoltaics. *J. Colloid Interface Sci.* **2017**, *489*, 28−37.
(20) Sygletou, M.; Petridis, C.; Kymakis, E.; Stratakis, E. Advanced Photonic Processes for Photovoltaic and Energy Storage Systems. *Adv. Mater.* **2017**, *29*, 1700335.
(21) Vailionis, A.; Gamaly, E. G.; Mizeikis, V.; Yang, W.; Rode, A. V.; Juodkazis, S. Evidence of Superdense Aluminium Synthesized by Ultrafast Microexplosion. *Nat. Commun.* **2011**, *2*, 1−6.
(22) Mintcheva, N.; Srinivasan, P.; Rayappan, J. B. B.; Kuchmizhak, A. A.; Gurbatov, S.; Kulinich, S. A. Room-Temperature Gas Sensing of Laser-Modified Anatase TiO_2 Decorated with Au Nanoparticles. *Appl. Surf. Sci.* **2020**, *507*, 145169.
(23) Chen, M.; Wang, D.; Liu, X. Direct Synthesis of Size-Tailored Bimetallic Ag/Au Nano- Spheres and Nano-Chains with Controllable Compositions by Laser Ablation of Silver Plate in HAuCl 4 solution. *RSC Adv.* **2016**, *6*, 9549−9553.
(24) Zhang, D.; Ma, Z.; Spasova, M.; Yelsukova, A. E.; Lu, S.; Farle, M.; Wiedwald, U.; Gökce, B. Formation Mechanism of Laser-Synthesized Iron−Manganese Alloy Nanopar- ticles, Manganese Oxide Nanosheets and Nanofi ers. *Part. Part. Syst. Charact.* **2017**, *34*, 1600225.
(25) Zhang, D.; Zhang, C.; Liu, J.; Chen, Q.; Zhu, X.; Liang, C. Carbon-Encapsulated Metal/Metal Carbide/Metal Oxide Core−Shell Nanostructures Generated by Laser Ab- lation of Metals in Organic Solvents. *ACS Applied Nano Materials* **2019**, *2*, 28−39.
(26) Shih, C.-Y.; Streubel, R.; Heberle, J.; Letzel, A.; Shugaev, M. V.; Wu, C.; Schmidt, M.; Gökce, B.; Barcikowski, S.; Zhigilei, L. V. Two Mechanisms of Nanoparticle Generation in Picosecond Laser Ablation in Liquids: The origin of the Bimodal Size Distribution. *Nanoscale* **2018**, *10*, 6900−6910.
(27) Lv, J.; Wu, S.; Tian, Z.; Ye, Y.; Liu, J.; Liang, C. Construction of PdO−Pd Interfaces Assisted by Laser Irradiation for Enhanced Electrocatalytic N 2 Reduction Reaction. *J. Mater. Chem. A* **2019**, *7*, 12627−12634.
(28) Alexander, D. T.; Forrer, D.; Rossi, E.; Lidorikis, E.; Agnoli, S.; Bernasconi, G. D.; Butet, J.; Martin, O. J.; Amendola, V. Electronic Structure-Dependent Surface Plasmon Resonance in Single Au−Fe Nanoalloys. *Nano Lett.* **2019**, *19*, 5754−5761.
(29) Tymoczko, A.; Kamp, M.; Rehbock, C.; Kienle, L.; Cattaruzza, E.; Barcikowski, S.; Amendola, V. One-Step Synthesis of Fe−Au Core−Shell Magnetic-Plasmonic Nanoparticles Driven by Interface Energy Minimization. *Nanoscale Horizons* **2019**, *4*, 1326−1332.
(30) Li, W.; Zhang, C.; Han, M.; Ye, Y.; Zhang, S.; Liu, Y.; Wang, G.; Liang, C.; Zhang, H. Ambient Electrosynthesis of Ammonia Using Core−Shell Structured Au@ C Catalyst Fabricated by One-Step Laser Ablation Technique. *ACS Appl. Mater. Interfaces* **2019**, *11*, 44186−44195.
(31) Shankar, P.; Ishak, M. H.; Padarti, J. K.; Mintcheva, N.; Iwamori, S.; Gurbatov, S. O.; Lee, J. H.; Kulinich, S. A. ZnO@ Graphene Oxide Core@ Shell Nanoparticles Prepared via One-Pot Approach Based on Laser Ablation in Water. *Appl. Surf. Sci.* **2020**, *531*, 147365.
(32) Chen, X.; Meng, C.; Wang, Y.; Zhao, Q.; Li, Y.; Chen, X.-M.; Yang, D.; Li, Y.; Zhou, Y. Laser-Synthesized Rutile TiO_2 with Abundant Oxygen Vacancies for Enhanced Solar Water Evaporation. *ACS Sustainable Chem. Eng.* **2020**, *8*, 1095−1101.
(33) Nastulyavichus, A. A.; Saraeva, I. N.; Rudenko, A. A.; Khmelnitskii, R. A.; Shakhmin, A. L.; Kirilenko, D. A.; Brunkov, P. N.; Melnik, N. N.; Smirnov, N. A.; Ionin, A. A.; Kudryashov, S. I. Multifunctional Sulfur-Hyperdoped Silicon Nanoparti- cles with Engineered Mid-Infrared Sulfur-Impurity and Free-Carrier Absorption. *Part. Part. Syst. Charact.* **2020**, *37*, 2000010.
(34) Liu, P.; Chen, H.; Wang, H.; Yan, J.; Lin, Z.; Yang, G. Fabrication of Si/Au Core/Shell Nanoplasmonic Structures with Ultrasensitive Surface-Enhanced Raman Scattering for Monolayer Molecule Detection. *J. Phys. Chem. C* **2015**, *119*, 1234−1246.
(35) Saraeva, I. N.; Luong, N. V.; Kudryashov, S. I.; Rudenko, A. A.; Khmelnitskiy, R. A.; Shakhmin, A. L.; Kharin, A. Y.; Ionin, A. A.; Zayarny, D. A.'b.; Tung, D. H.; Duong, P. V.; Minh, P. H. Laser Synthesis of Colloidal Si@ Au and Si@ Ag Nanoparticles in Water via Plasma-Assisted Reduction. *J. Photochem. Photobiol., A* **2018**, *360*, 125−131.
(36) Wang, J.-Q.; Xi, C.; Wang, M.; Shang, L.; Mao, J.; Dong, C.-K.; Liu, H.; Kulinich, S. A.; Du, X.-W. Laser-Generated Grain Boundaries in Ruthenium Nanoparticles for Boosting Oxygen Evolution Reaction. *ACS Catal.* **2020**, *10*, 12575−12581.
(37) Rajabalinia, N.; Hamzehlou, S.; Modin, E.; Chuvilin, A.; Leiza, J. R.; Asua, J. M. Coupling HAADF-STEM Tomography and Image Reconstruction for the Precise Characterization of Particle Morphology of Composite Polymer Latexes. *Macromolecules* **2019**, *52*, 5298−5306.
(38) Cardinal, M. F.; Vander Ende, E.; Hackler, R. A.; McAnally, M. O.; Stair, P. C.; Schatz, G. C.; Van Duyne, R. P. Expanding Applications of SERS through Versatile Nanomaterials Engineering. *Chem. Soc. Rev.* **2017**, *46*, 3886−3903.
(39) Palik, E. D. *Handbook of Optical Constants of Solids*; Academic Press: 1998; Vol. 3.
(40) Liu, L.; Chen, X. Titanium Dioxide Nanomaterials: Self-Structural Modifi. *Chem. Rev.* **2014**, *114*, 9890−9918.
(41) Checcucci, S.; Bottein, T.; Claude, J.-B.; Wood, T.; Putero, M.; Favre, L.; Gurioli, M.; Abbarchi, M.; Grosso, D. Titania-Based Spherical Mie Resonators Elaborated by High- Throughput Aerosol Spray: Single Object Investigation. *Adv. Funct. Mater.* **2018**, *28*, 1801958.
(42) Mao, P.; Liu, C.; Song, F.; Han, M.; Maier, S. A.; Zhang, S. Manipulating Disordered Plasmonic Systems by External Cavity with Transition from Broadband Absorption to Reconfigurable Reflection. *Nat. Commun.* **2020**, *11*, 1−7.
(43) Langer, J.; Jimenez de Aberasturi, D.; Aizpurua, J.; Alvarez-Puebla, R. A.; Augui'e, B.; Baumberg, J. J.; Bazan, G. C.; Bell, S. E.; Boisen, A.; Brolo, A. G.; et al. Present and future of surface-enhanced Raman scattering. *ACS Nano* **2020**, *14*, 28−117.
(44) Liu, Y.-C.; Yu, C.-C.; Wang, C.-C.; Juang, L.-C. New Application of Photocatalytic TiO_2 Nanoparticles on the Improved Surface-Enhanced Raman Scattering. *Chem. Phys. Lett.* **2006**, *420*, 245−249.
(45) Cong, S.; Yuan, Y.; Chen, Z.; Hou, J.; Yang, M.; Su, Y.; Zhang, Y.; Li, L.; Li, Q.; Geng, F.; Zhao, Z. Noble Metal-Comparable SERS Enhancement from Semiconducting Metal Oxides by Making Oxygen Vacancies. *Nat. Commun.* **2015**, *6*, 1−7.
(46) Kriegel, I.; Scotognella, F.; Manna, L. Plasmonic Doped Semiconductor Nanocrystals: Properties, Fabrication, Applications and Perspectives. *Phys. Rep.* **2017**, *674*, 1−52.

https://dx.doi.org/10.1021/acsami.0c20463
ACS Appl. Mater. Interfaces 2021, 13, 6522−6531

(47) Balčytis, A.; Nishijima, Y.; Krishnamoorthy, S.; Kuchmizhak, A.; Stoddart, P. R.; Petrůškevičius, R.; Juodkazis, S. From Fundamental Toward Applied SERS: Shared Principles and Divergent Approaches. *Adv. Opt. Mater.* **2018**, *6*, 1800292.
(48) Mitsai, E.; Kuchmizhak, A.; Pustovalov, E.; Sergeev, A.; Mironenko, A.; Bratskaya, S.; Linklater, D.; Balčytis, A.; Ivanova, E.; Juodkazis, S. Chemically Non-Perturbing SERS Detection of a Catalytic Reaction with Black Silicon. *Nanoscale* **2018**, *10*, 9780−9787.
(49) De Angelis, F.; et al. Breaking the Diffusion Limit with Super-Hydrophobic Delivery of Molecules to Plasmonic Nanofocusing SERS Structures. *Nat. Photonics* **2011**, *5*, 682−687.
(50) Yang, S.; Dai, X.; Stogin, B. B.; Wong, T.-S. Ultrasensitive Surface-Enhanced Ra- man Scattering Detection in Common Fluids. *Proc. Natl. Acad. Sci. U. S. A.* **2016**, *113*, 268−273.
(51) Pavliuk, G.; Pavlov, D.; Mitsai, E.; Vitrik, O.; Mironenko, A.; Zakharenko, A.; Kulinich, S. A.; Juodkazis, S.; Bratskaya, S.; Zhizhchenko, A.; Kuchmizhak, A. Ultrasensitive SERS-Based Plasmonic Sensor with Analyte Enrichment System Produced by Direct Laser Writing. *Nanomaterials* **2020**, *10*, 49.
(52) Chen, X.; Zhao, D.; Liu, K.; Wang, C.; Liu, L.; Li, B.; Zhang, Z.; Shen, D. Laser- Modified Black Titanium Oxide Nanospheres and their Photocatalytic Activities under Visible Light. *ACS Appl. Mater. Interfaces* **2015**, *7*, 16070−16077.
(53) Zhou, L.; Tan, Y.; Wang, J.; Xu, W.; Yuan, Y.; Cai, W.; Zhu, S.; Zhu, J. 3D Self- Assembly of Aluminium Nanoparticles for Plasmon-Enhanced Solar Desalination. *Nat. Photonics* **2016**, *10*, 393−398.
(54) Zhao, F.; Guo, Y.; Zhou, X.; Shi, W.; Yu, G. Materials for Solar-Powered Water Evaporation. *Nature Reviews Materials* **2020**, *5*, 388−401.
(55) Neumann, O.; Urban, A. S.; Day, J.; Lal, S.; Nordlander, P.; Halas, N. J. Solar Vapor Generation Enabled by Nanoparticles. *ACS Nano* **2013**, *7*, 42−49.
(56) Jin, H.; Lin, G.; Bai, L.; Zeiny, A.; Wen, D. Steam Generation in a Nanoparticle-Based Solar Receiver. *Nano Energy* **2016**, *28*, 397−406.
(57) Arunkumar, T.; Wang, J.; Denkenberger, D. Capillary Flow-Driven Efficient Nanomaterials for Seawater Desalination: Review of Classification, Challenges, and Future perspectives. *Renewable Sustainable Energy Rev.* **2021**, *138*, 110547.
(58) Pang, Y.; Zhang, J.; Ma, R.; Qu, Z.; Lee, E.; Luo, T. Solar−Thermal Water Evaporation: A Review. *ACS Energy Letters* **2020**, *5*, 437−456.
(59) Wu, S.-L.; Chen, H.; Wang, H.-L.; Chen, X.; Yang, H.-C.; Darling, S. B. Solar-Driven Evaporators for Water Treatment: Challenges and Opportunities. *Environmental Science: Water Research & Technology* **2021**, *7*, 24−39.

https://dx.doi.org/10.1021/acsami.0c20463
ACS Appl. Mater. Interfaces 2021, 13, 6522−6531